An analysis of 1D finite-volume methods for geophysical problems on refined grids

Paul A. Ullrich *, Christiane Jablonowski

Department of Atmospheric, Oceanic and Space Sciences, Space Research Building, University of Michigan, 2455 Hayward St., Ann Arbor, MI 48109, USA

ARTICLE INFO

ABSTRACT

This paper examines high-order unstaggered symmetric and upwind finite-volume discretizations of the advection equation in the presence of an abrupt discontinuity in grid resolution. An approach for characterizing the initial amplitude of a parasitic mode as well as its decay rate away from a grid resolution discontinuity is presented. Using a combination of numerical analysis and empirical studies it is shown that spurious parasitic modes, which are artificially generated by the resolution discontinuity, are mostly undamped by symmetric finite-volume schemes but are quickly removed by upwind and semi-Lagrangian integrated mass (SLIM) schemes. Slope/curvature limiting is insufficient to completely remove these modes, especially at low forcing frequencies where the incident wave can act as a carrier of the parasitic mode. Increasing the order of accuracy of the reconstruction at the grid interface is effective at removing noise from the lowest-frequency incident modes, but insufficient at high frequencies. It is shown that this analysis can be extended to the 1D linear shallow-water equations via Riemann invariants.

1. Introduction

The atmosphere and ocean are two facets of a vast nonlinear system that works on a broad range of interacting scales. Models are an invaluable tool for enhancing our understanding of this system, but the enormity of the problem-spanning the entirety of the Earth's surface-is at the edge of our present computational power. In order to meet growing demand for fine-scale simulations, the next generation of atmospheric models will likely need to rely on adaptive mesh refinement (AMR) in order to properly capture features of interest. A dynamically adaptive model, for instance, would be capable of hurricane tracking and modeling on a global scale, and would enhance our knowledge of mountain waves and extreme weather events. However, the benefits of adaptively refined grids do not come without a fair share of problems. Perhaps the most significant of these problems, in the context of geophysical modeling, is related to the mathematical handling of wave phenomena at coarse–fine grid boundaries. Except for a handful of numerical methods, most schemes allow wave groups to be spuriously reflected at grid resolution interfaces (see, for example, [37]). This type of wave reflection is attributed to sudden changes in the numerical structure of the system, analogous to changes in the physical characteristics of the system.

As shown by Vichnevetsky [37] and later by Vichnevetsky and Turner [38], the significance of wave reflection increases substantially when the grid resolution is varied abruptly. As a consequence, many approaches (see, for example, [9,11,30]) instead rely on a smooth variation of the grid between coarse and fine regions. However, abruptly-varying grids generally perform better on parallel architectures when dynamic refinement is desired; in this case, dynamic grid refinement in a compact region can be performed without having to reconstruct the grid over a wide regional or global scale (which is necessary

* Corresponding author. Tel.: +1 734 272 2702; fax: +1 734 763 0437.
  E-mail addresses: paullric@umich.edu (P.A. Ullrich), cjablono@umich.edu (C. Jablonowski).

if smooth variation of the grid is required). Although these block-adaptive grids have been long used for astrophysical, aerospace and other computational fluid dynamics problems (see, for example, [1,2]), they were only first applied to geophysical limited area models by Skamarock et al. [29] and Skamarock and Klemp [28]. More recently, these methods have been applied in spherical geometry by Jablonowski et al. [16,17]. Hence, our approach in this paper is to consider only grids with abrupt variation in resolution.

To a close approximation, the atmosphere and ocean are in a state of geostrophic and hydrostatic balance. For geophysical flows, departures from geostrophy are approximately linear. The Mach number of these flows is generally much less than one, and shock waves are not present. It is here where linear numerical discretizations are the most relevant, since slope limiters are generally not required to ensure positivity of the thermodynamic variables. Long-term simulations of geostrophic flows also require perhaps the most stringent conservation constraints since a slow escape of air from the atmosphere on the order of the scheme's truncation error can lead to substantial atmospheric loss over time.

Although many previous papers have discussed the issue of wave reflection due to a discontinuity in grid resolution, these works have not focused on the issue of wave reflection in dissipative finite-volume methods. In this case, energy is not conserved over time, and so it is uncertain whether previous results, which have been derived in the case of zero energy dissipation, will still hold. Hence, it is our objective in this paper to use mathematical analysis and numerical experimentation to determine which unstaggered dissipative finite-volume methods are best suited for geophysical modeling in the presence of a refined grid.

Before proceeding, we briefly discuss the wave reflection properties of other approaches. Frank and Reich [12] demonstrated that the Box scheme is free of spurious reflections, but this scheme does not easily generalize to multiple dimensions and is implicit in a periodic domain. Further, purely upwind schemes, such as the first-order Godunov scheme, the discontinuous Galerkin (DG) scheme and spectral-volume methods, all of which do not use downstream information, are free from spurious wave reflection when applied to the advection equation. Nonetheless, these methods still suffer from nonlinear wave reflection when applied to the 1D shallow-water equations, for instance.

The foundation for our analysis will be the 1D advection equation, which describes the motion of a tracer field $q(x,t)$ in the presence of an underlying velocity field u. In its simplest form, this equation reads

$$\frac{\partial q}{\partial t} + u \frac{\partial q}{\partial x} = 0. \tag{1}$$

For simplicity, much of our analysis will be for the case that $u = \text{const} > 0$.

This paper is organized as follows. First, we present a framework for the set of finite-volume methods we will consider in Section 2, and give some of their numerical properties. The results of a set of wave-reflection experiments are then given in Section 3. In Section 4 we introduce the shallow-water equations and linearized shallow-water equations, and show their connection to the advection equation. Lastly, our conclusions are presented in Section 5. Note that throughout this paper we will be making use of dimensionless length and time units.

2. Numerical discretizations

Numerous methods have been devised for the construction of finite-volume schemes, and all have their benefits and disadvantages. The method-of-lines approach is perhaps the most popular for constructing high-order finite-volume methods that are applicable to general systems of equations. Under this framework, a spatial sub-grid-scale reconstruction is combined with a numerical flux function to provide a discretization of the spatial component of the differential equation, which is then combined with a timestepping scheme that guarantees stability and accuracy when integrating forward in time. Timestepping schemes vary substantially in their properties, but must be chosen so that the eigenvalues of the spatial operator fit within the stability region of the timestepping scheme. We consider three types of finite-volume methods constructed under this framework:

- *Symmetric finite-volume.* If we assume continuity of our solution between elements we can directly reconstruct the value of the underlying field at edge-points. An interior reconstruction, which is necessary for evaluating source terms, is then obtained from the edge-values and value of the cell-averaged scalar field. Once the initial approximation is made, monotonicity constraints can be applied, which may cause the field to again become discontinuous at edges and hence require the solution of a Riemann problem. This approach does not rely more strongly on upwind-biased information, and so leads to a spatial discretization which is symmetric about the element being updated. The simplest symmetric finite-volume method is the so called central-in-space discretization, which has been thoroughly studied in the context of grid reflection (see, for example, [32,37,38]). It is obtained by assuming the value of the scalar field at each edge is simply the average of the values of neighbouring elements.
- *Upwind finite-volume.* The Monotone Upstream-centered Schemes for Conservation Laws (MUSCL) formalism of van Leer [36] provides a mechanism for computing a sub-grid-scale reconstruction via a local reconstruction obtained from adjacent cell-averaged values. When evaluated at edge points, these reconstructions can then act as left and right states that are then used to solve a Riemann problem. Slope limiters can also be applied in the reconstruction step to enforce monotonicity and limit spurious oscillations. This approach leads to the upwind family of finite-volume schemes, so-named

because they rely more heavily on information propagated in the direction of the fluid motion. Unstaggered high-order upwind finite volume schemes have been recently shown to be viable for shallow-water models on the sphere by Ullrich et al. [33].

- *Semi-Lagrangian integrated-mass (SLIM) finite-volume methods.* A popular method that has been widely adopted for discretizations of the advection equation is the so-called semi-Lagrangian (SL) approach. This method comes in two flavors–namely, forward SL and backward SL. In the forward SL approach, the velocity field is used to deform the grid, which is then remapped back to the original cell positions. In the backward approach, the velocity field is first evolved to time $n + 1$. The evolved velocity field is then used to "devolve" the grid cells at time $n + 1$ into a deformed grid that represents the locations of these cells at time n. Finally, the original grid information is remapped onto the deformed grid, giving new cell averages. These two approaches are identical for the 1D advection equation with u = const. Semi-Lagrangian methods are a physically motivated treatment of the advection equation, and have effectively no timestep limit (but accuracy degrades substantially for large timesteps and non-constant flow fields). Nonetheless, there is some difficulty in adapting this method to general hyperbolic systems. An analysis of SLIM schemes can be found in Laprise and Plante [19]. Examples of this approach include Fromm's scheme [13], the advective form of the piecewise-parabolic method presented by Colella and Woodward [8] and, in higher dimensions, the recently introduced CSLAM transport scheme of Lauritzen et al. [20].

2.1. Diffusion, phase velocity and group velocity

An excellent tool for describing the properties of numerical discretizations is wave-mode analysis, which forms the backbone of our study of spurious wave reflection. In particular, this approach has been successfully applied by Trefethen [32] and Grotjahn and O'Brien [14] in the analysis of numerical methods for hyperbolic equations.

In general, any linear partial differential equation with constant coefficients supports wave-like solutions of the form

$$q(x,t) = \hat{q}\exp(i(kx - \omega t)), \tag{2}$$

where $q(x,t)$ denotes the state variable in physical space, $\hat{q}$ is the corresponding amplitude, k is the wave number and ω is the frequency. If we substitute this solution into (1) we obtain a *dispersion relation* of the form

$$\omega(k) = uk. \tag{3}$$

These modes propagate with speed

$$c_p(k) = \frac{\omega(k)}{k}, \tag{4}$$

which is known as the *phase speed*. The evolution of a wave packet however, is determined by the *group speed*, defined via

$$c_g(k) = \frac{\partial \omega}{\partial k}. \tag{5}$$

It is well-known (see, for example, Brillouin [4]) that the group speed is the speed at which energy propagates in a system, as well as the speed associated with a traveling wave packet. In the case of the advection equation, these velocities are equivalent and given by $c_p = c_g = u$.

Linear discretizations of (1) similarly support wave modes of the form (2) but only allow us to roughly approximate the correct dispersion relation (3). When analyzing these numerical methods we will assume an uniform spatial grid, defined at discrete points via

$$x_j = j\Delta x, \quad \text{and} \quad t_n = n\Delta t, \tag{6}$$

where Δx and Δt are the element width and timestep, respectively, and j and n are spatial and temporal indices. Hence, wave-like solutions (2) take the form

$$q_j^n = \hat{q}\exp(i(kj\Delta x - \omega n\Delta t)), \tag{7}$$

where $k\Delta x$ is the normalized wave number, whose real component takes on values in the range $[0,\pi]$. On substituting this expression into a discrete numerical scheme, we obtain the *numerical dispersion relation*, which describes the relationship between ω and k and usually incorporates the dimensionless Courant–Friedrichs–Lewy (CFL) number

$$K = \frac{u\Delta t}{\Delta x}. \tag{8}$$

The numerical dispersion relation is a powerful tool for describing the properties of a numerical method:

- For two time-level schemes, such as forward Euler, backward Euler, Crank–Nicolson and all Runge–Kutta schemes, every value of k is associated with a single value ω. For three time-level schemes, such as the Leapfrog scheme, every value of k is associated with two values of ω.

- The imaginary component of $\omega(k)$ describes the growth rate of the mode k. Von Neumann stability [6] is obtained by guaranteeing that $\mathrm{Im}\,(\omega) \leqslant 0$ for all real wave numbers. Stable numerical schemes which satisfy $\mathrm{Im}(\omega(k)) < 0$ for some k are known as *diffusive* (or *dissipative*). Note that the advection equation is naturally non-diffusive, so any non-zero diffusivity leads to *diffusive error*. The *amplification factor* after one timestep is then defined as

$$A_{\Delta t} = \exp(\mathrm{Im}(\omega(k))\Delta t). \tag{9}$$

However, $A_{\Delta t}$ is not desirable for describing the diffusivity of a scheme over a range of CFL numbers, since schemes with smaller timestep Δt must be applied multiple times to advance to the same time as schemes with larger Δt. Hence, one can alternatively describe diffusivity in terms of the *normalized amplification factor A*, defined for a fixed wavenumber k by

$$A = \exp(\mathrm{Im}(\omega(k))T), \tag{10}$$

where T is some fixed time. In the following analysis we choose $T = 1$ for simplicity.

- In general, a numerical dispersion relation will yield a frequency whose real component is nonlinearly dependent on k. In this case, the scheme will be *dispersive*, indicating that different wave numbers will travel at different phase speeds. The advection equation is non-dispersive, since ω and k are linearly related, however, numerical discretizations generally introduce *dispersive error* in the form of a nonlinear dispersion relation. The dispersive characteristics of a numerical method can be effectively described in terms of the phase velocity and group velocity, which are obtained from the numerical dispersion relation, when combined with (4) and (5). Since a numerical method can also be dissipative, we substitute $\mathrm{Re}(\omega)$ for ω in these relationships, which yields the numerical phase velocity and group velocity.

Note that group velocity analysis only applies directly for nondiffusive schemes, since diffusivity introduces a wavenumber-dependent attenuation of different wave modes. As a consequence, wave packets can lose their distinctive shape over time as certain wave modes are diffused from the simulation. However, the results of group velocity analysis will still hold approximately as long as the wave packet is composed of waves with similar diffusion rates.

2.2. Linear discretizations

In this paper we focus our attention on high-order linear discretizations. Namely, we are interested in spatial semi-discretizations of the advection Eq. (1) that take the form

$$\frac{\partial q_j}{\partial t} = \sum_{m=-\ell}^{r} c_m q_{j+m}, \tag{11}$$

where the coefficients c_m are purely a function of the grid spacing Δx, timestep Δt and advection speed u (possibly via the CFL number). Here ℓ and r denote the number of leftward-elements and rightward-elements in the semi-discrete stencil. For simplicity, in this paper we only analyze methods with $r \leqslant \ell = 2$, which leads to a stencil with at most five elements. Conservation is guaranteed by utilizing the finite-volume framework, which requires that all of the schemes can be written in the form

$$\frac{\partial q_j}{\partial t} = -\frac{F^*_{j+1/2}(\ldots, q_{j-1}, q_j, q_{j+1}, \ldots) - F^*_{j-1/2}(\ldots, q_{j-1}, q_j, q_{j+1}, \ldots)}{\Delta x} \tag{12}$$

for a numerical flux function $F^*_{j+1/2}$. The numerical flux functions are defined at cell edges, which are denoted by half-indices.

When combined with an appropriate two-time-level explicit timestepping operator, the spatial semi-discretization (11) then leads to a complete discretization of the advection equation that we can write as

$$q_j^{n+1} = \sum_{m=-\ell \cdot s}^{r \cdot s} C_m q_{j+m}^n, \tag{13}$$

where the C_m are again purely functions of the grid spacing, timestep and advection speed. Here s denotes the number of stages used by the timestepping operator (for multistage schemes, such as the Runge–Kutta methods).

To determine the numerical dispersion relation for the scheme (13), we simply substitute (7) and solve for ω, obtaining

$$\mathrm{Re}(\omega) = -\frac{1}{\Delta t} \arctan\left[\frac{\sum_{m=-\ell \cdot s}^{r \cdot s} C_m \sin(km\Delta x)}{\sum_{m=-\ell \cdot s}^{r \cdot s} C_m \cos(km\Delta x)}\right]. \tag{14}$$

Solutions to this equation are not unique, and the choice of an appropriate branch cut for the arctan function can lead to some confusion. Herein we will take the branch cut that gives $\omega(0) = 0$ and otherwise is a continuous function of k.

2.3. The $2\Delta x$ mode problem

Symmetric finite-volume (semi-) discretizations of the advection equation satisfy the property $c_m = -c_{-m}$, which usually arises from the application of a centered differencing operator within each element. They are characterized by low diffusivity

and consistent behaviour regardless of CFL number, but suffer from the so-called $2\Delta x$ mode problem; namely, under such a semi-discretization both the constant field q_j = const. and the $2\Delta x$ mode $q_j = (-1)^j$ satisfy

$$\frac{\partial q_j}{\partial t} = 0, \tag{15}$$

implying that both modes are invariant in time. Thus, under a symmetric finite-volume method, the constant mode and $2\Delta x$ mode are indistinguishable, regardless of the size of the stencil and choice of temporal discretization. As a consequence, this mode will feature both zero diffusion and zero phase velocity when simulating the advection equation, and so any nonlinear effects or source terms which contribute energy to this scale will not be dissipated. The result is "checkerboarding" of the state variables under this operator (see, for example, [26]).

Upwind finite-volume (semi-) discretizations are always upwind biased, satisfying $r < \ell$. This criterion implies that more information is drawn from the upwind direction as the flow evolves. In general, these methods do not suffer from the $2\Delta x$ mode problem, but may possess high-frequency wave modes which are weakly damped, usually at specific CFL numbers.

2.4. The gas dynamics form of the piecewise-parabolic method (PPM)

The gas dynamics form of the piecewise-parabolic method (PPM) of Colella and Woodward [8] (Chapter 3) is a high-order symmetric discretization that, for a locally smooth field q, estimates the field at edge points via the central reconstruction

$$q_{j+1/2} = \frac{-q_{j-1} + 7q_j + 7q_{j+1} - q_{j+2}}{12} + O(\Delta x^4). \tag{16}$$

Because the field is assumed continuous at edge points (with no limiter applied), the numerical flux can be computed directly without applying a Riemann solver,
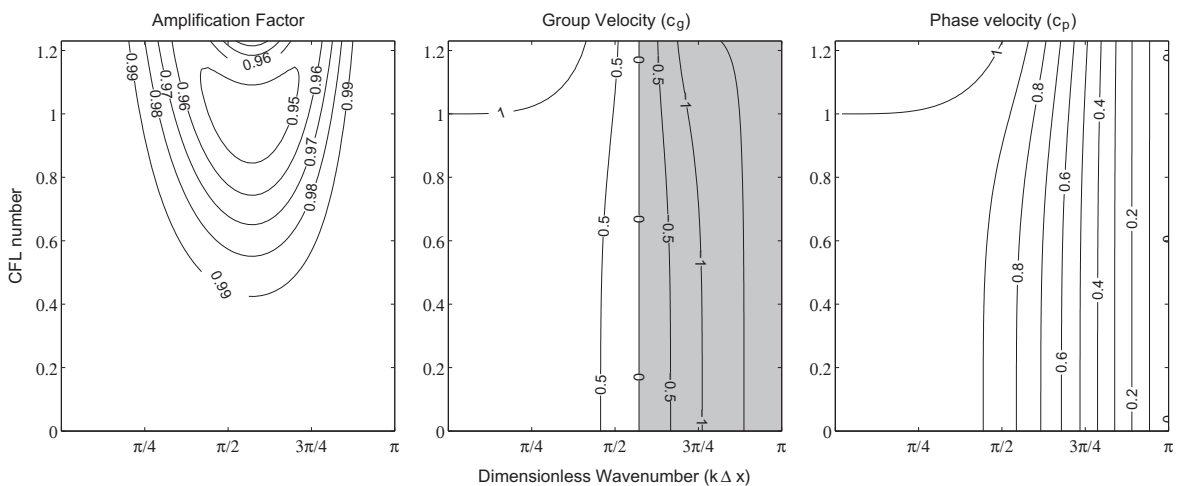
$$F^*_{j+1/2} = u \cdot q_{j+1/2}. \tag{17}$$

This choice leads to the semi-discretization

$$\frac{\partial q_j}{\partial t} = -\frac{K}{\Delta t}\left(\frac{1}{12}q_{j-2} - \frac{8}{12}q_{j-1} + \frac{8}{12}q_{j+1} - \frac{1}{12}q_{j+2}\right), \tag{18}$$

where the RHS of (18) is exactly the fourth-order symmetric approximation to $\partial q/\partial x$ centered at element j. The eigenvalues of this spatial operator are purely imaginary, and so must be paired with at least a three-stage third-order Runge–Kutta (RK3) timestep. Doing so, we obtain a scheme that is stable up to $K \leqslant 1.26$.

We plot the normalized amplification factor, group velocity and phase velocity associated with this scheme in Fig. 1. Observe, in particular, that this scheme supports waves with negative group velocity, leading to a maximum negative group velocity of $-5/3$ at $k\Delta x = \pi$. The range of dimensionless wavenumbers $k\Delta x \in [\pi/2, \pi]$ corresponds to the waves with wavelength between $4\Delta x$ and $2\Delta x$. Most waves in this range travel with negative group speeds and so are not truthfully represented by the numerical scheme. Note that the phase velocity also drops to zero at $k\Delta x = \pi$, whereas at this wavenumber the amplification factor is exactly 1 regardless of CFL number. As mentioned previously, this implies that the $2\Delta x$ mode is an undamped "standing wave" that is retained by the numerical method.

Fig. 1. Contour plots showing diffusive and dispersive characteristics associated with PPM with RK3 timestep. Here Δt is varied so as to span to CFL range $[0, 1.26]$ with constant wave speed $u = 1$ and fixed Δx. Gray regions in the group velocity plot indicate regions of negative group velocity.

2.5. A second-order upwind (FV2) scheme

A linear sub-grid-scale reconstruction was adopted by van Leer [34,36] for shock-hydrodynamics problems, where the derivative was obtained via a nonlinear limiting procedure. Without a strict monotonicity constraint, we can instead forego the limiting procedure and hence obtain a linear second-order-accurate upwind scheme. A sub-grid-scale reconstruction of the form

$$\tilde{q}_j(x) = q_j + (x - x_j)Dq_j, \tag{19}$$

is computed in each cell, where Dq_j denotes the numerical approximation to the first derivative, obtained from the central-difference formula

$$Dq_j = \frac{q_{j+1} - q_{j-1}}{2\Delta x}. \tag{20}$$

Since this reconstruction is discontinuous at cell edges we must use a Riemann flux operator, taken simply to be the upwind flux

$$F^*_{j+1/2} = u\tilde{q}_j\left(x_j + \frac{\Delta x}{2}\right). \tag{21}$$

After simplifying, the evolution equation reads

$$\frac{\partial q_j}{\partial t} = -\frac{K}{\Delta t}\left(\frac{1}{4}q_{j-2} - \frac{5}{4}q_{j-1} + \frac{3}{4}q_j + \frac{1}{4}q_{j+1}\right), \tag{22}$$

This scheme is unstable under a forward Euler timestep, but stable for Runge–Kutta operators of at least second order. Making use of the two-stage second-order Runge–Kutta scheme (RK2), we obtain a discretization that is stable for $K \leqslant 1$.

We plot the normalized amplification factor, group velocity and phase velocity associated with this scheme in Fig. 2. In particular, observe that for this scheme wave modes which are propagated with negative group velocities are also modes which experience strong diffusion. This result was previously obtained by Karni [18], who observed that even in the limit of vanishing CFL number wave groups were not permitted to propagate backwards in upwind schemes. A singularity can also be observed in the group velocity and phase velocity plots, corresponding to the point where the amplification factor is identically zero. The solid line that extends to the right of the singularity in the phase velocity plot is a discontinuity in the branch cut when evaluating the frequency ω from (14). Comparing this scheme against PPM in Fig. 1, we observe that the FV2 scheme possesses a much more complicated structure and introduces stronger diffusion at high wavenumbers. As with PPM, the $2\Delta x$ mode is a standing mode with non-zero group velocity; however, unlike in PPM, this mode is strongly damped at all but the largest of the stable CFL numbers. In the nonlinear case this analysis suggests bounding the CFL number by 0.9 so as to prevent artificial enhancement of this mode against the background field.

2.6. A third-order upwind (FV3p3) scheme

Extending on the ideas of van Leer [34,35], we make use of a sub-grid-scale reconstruction of the form

$$\tilde{q}_j(x) = q_j + (x - x_j)Dq_j + \left((x - x_j)^2 - \frac{\Delta x^2}{12}\right)\left(\frac{1}{2}D^2q_j\right), \tag{23}$$
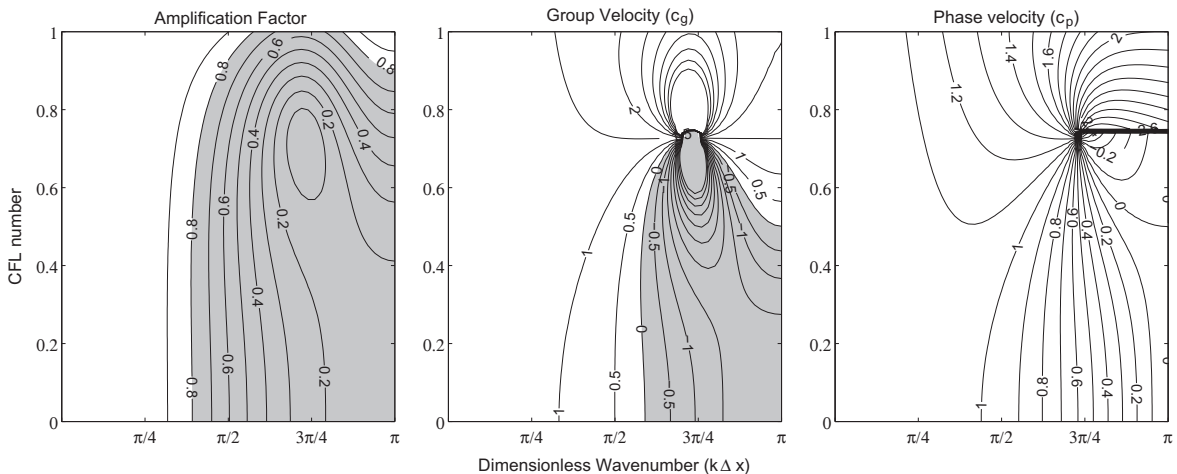
Fig. 2. Contour plots showing diffusive and dispersive characteristics associated with the FV2 scheme with RK2 timestep. Here Δt is varied so as to span to CFL range [0,1] with constant wave speed $u = 1$. Gray regions indicate regions of significant damping on the plot of the amplification factor ($A \leqslant 0.8$) and negative (backwards propagating) group velocities on the plot of the group velocity.

where x_j is the centerpoint of element j and $D q_j$ and $D^2 q_j$ denote numerical approximations to the first and second derivatives of the field q in element j, obtained from

$$Dq_j = \frac{q_{j+1} - q_{j-1}}{2\Delta x}, \quad \text{and} \quad D^2 q_j = \frac{q_{j+1} - 2q_j + q_{j-1}}{\Delta x^2}. \tag{24}$$

As with the FV2 scheme, we compute edge fluxes via the upwind flux (21), leading to the evolution equation

$$\frac{\partial q_j}{\partial t} = -\frac{K}{\Delta t} \left(\frac{1}{6} q_{j-2} - q_{j-1} + \frac{1}{2} q_j + \frac{1}{3} q_{j+1} \right). \tag{25}$$

This scheme is unstable under both the forward Euler method and RK2 timestep since the eigenvalues of the spatial operator closely shadow the imaginary axis near the origin. Hence, we will combine this spatial stencil with the third-order Runge–Kutta (RK3) scheme, leading to a scheme that is stable up to $K \leqslant 1.63$.

We plot the normalized amplification factor, group velocity and phase velocity associated with this scheme in Fig. 3. As with the FV2 scheme (see Fig. 2), the behaviour is complicated for wavenumbers in the range $[\pi/2, \pi]$, featuring two singularities due to the presence of a zero amplification factor. Again we observe a similar branch cut discontinuity in the phase velocity plot. Interestingly, the group velocity is positive for virtually all wavenumbers at $K \geqslant 1.32$. Also, the $2\Delta x$ mode always experiences significant diffusion under this scheme, whereas the $3\Delta x$ mode ($k\Delta x = 2\pi/3$) is relatively undamped at high CFL numbers. Diffusion in this method is comparable to the FV2 scheme, with slightly stronger diffusion at CFL numbers greater than about 0.6.

2.7. A third-order semi-Lagrangian integrated-mass (SLIM3p3) scheme

The third-order semi-Lagrangian scheme we will analyze is based on the discontinuous piecewise-parabolic reconstruction of Laprise and Plante [19]. In this case we again make use of a reconstruction of the form (23) and (24), except now we apply the SLIM methodology to compute fluxes by integrating upstream from each cell edge. For CFL numbers in the range $0 \leqslant K \leqslant 1$ the numerical flux function then takes the form

$$F^*_{j+1/2} = \frac{1}{\Delta t} \int_{x_j + \Delta x/2 - u\Delta t}^{x_j + \Delta x/2} \tilde{q}(x') dx' = \frac{u}{6} \left[(K^2 - 1)q_{j-1} - (K+1)(2K-5)q_j + (K-1)(K-2)q_{j+1} \right]. \tag{26}$$

The integrated transport scheme then takes the form

$$\frac{\partial q_j}{\partial t} = -\frac{K}{\Delta t} \left[-\frac{1}{6}(K^2 - 1)q_{j-2} + \frac{1}{2}(K+1)(K-2)q_{j-1} - \frac{1}{2}(K^2 - 2K - 1)q_j + \frac{1}{6}(K-1)(K-2)q_{j+1} \right]. \tag{27}$$

As stated earlier, SLIM methods can be extended to have an arbitrarily large CFL number if the integration is applied only to elements that overlap the Lagrangian control volume (see, for example, Lauritzen et al. [20]).
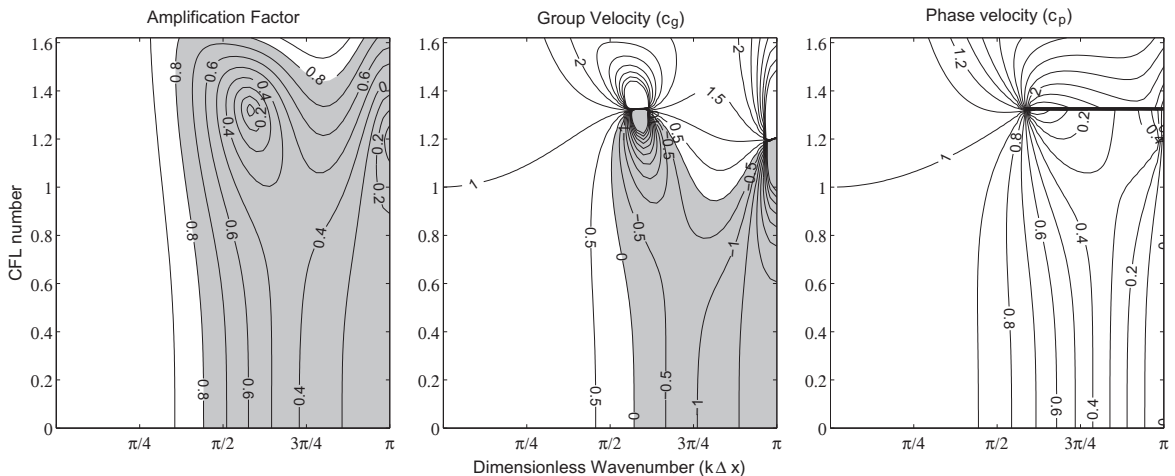

Fig. 3. As Fig. 2 except with the FV3p3 scheme with RK3 timestep. Here we span the CFL number over the range [0,1.63].
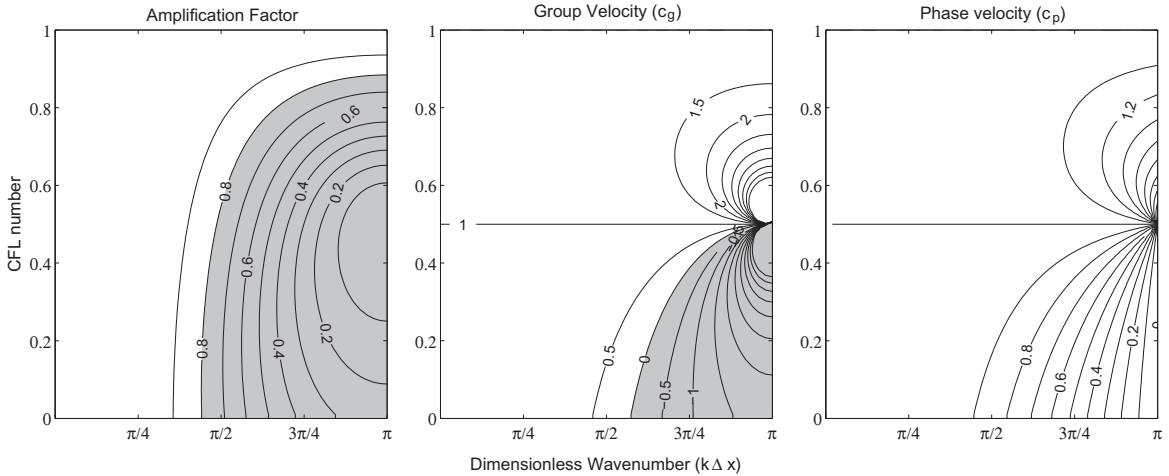
Fig. 4. As Fig. 2 except with the SLIM3p3 scheme with forward Euler timestep. Here we span the CFL number over the range [0, 1.0].

Unlike (18), (22) and (25), the SLIM framework leads to an evolution equation that is nonlinear in K. This scheme is stable if combined with a forward Euler timestep and further is exact for $K = 1$. Unlike the previous schemes, we do not recommended combining this scheme with a Runge–Kutta timestep since the resulting scheme is highly diffusive.

We plot the normalized amplification factor, group velocity and phase velocity associated with this scheme in Fig. 4. The remapping step in the SLIM framework is responsible for the diffusivity of the scheme, and leads to an amplification factor of zero at $k = \pi$ and $K = \frac{1}{2}$ (with a corresponding singularity in the group velocity). As with the upwind finite-volume schemes, waves in the region of negative group velocity also experience strong diffusion. Notably, diffusion in this scheme is weaker than for the corresponding upwind schemes.

3. Wave reflection

In this section we tackle the problem of spurious wave reflection due to a grid resolution discontinuity. In Section 3.1, we introduce our test environment for spurious wave reflection. We analyze the decay rate of spurious modes in Section 3.2 and the initial amplitude of a reflected wave in Section 3.3. We present several reflected wave tests using a symmetric FV scheme in Section 3.4 with and without a slope limiter. A similar analysis is performed for upwind finite-volume schemes in Section 3.5 and for SLIM finite-volume schemes in Section 3.6.

Spurious wave reflection in the advection equation can be attributed to an artificial transfer of energy from forward-propagating physical modes into spurious backward-propagating parasitic modes. When a forward-propagating wave packet hits a resolution discontinuity, frequency must be conserved across the interface, but errors are accumulated at all wave numbers with the supported frequency. Certain modes are then propagated backwards relative to the flow. This type of wave reflection can occur even when a scheme does not possess wave modes with negative group velocity, and depends largely on the amount of downstream information that is used in the evolution equations; it is a linear effect, and so tends to be the dominant source of error even among nonlinear differential equations.

3.1. Wavemaker driven grid reflection

Wave-like solutions are not, in general, eigenfunctions of the discrete update equations on a grid with a resolution discontinuity. However, if we neglect boundary conditions, they are eigenfunctions of the update equations on each uniformly spaced grid.

In order to analyze wave reflection at grid resolution discontinuities, we follow the approach proposed by Trefethen [32]. Under this simplified model, the advection equation is simulated over a domain $x = [0, 1]$ with a grid resolution discontinuity introduced at $x = 1/2$. In the regions $x = [0, 1/2]$ and $x = [1/2, 1]$ we make use of discrete grid spacing Δx_f (on the fine grid) and Δx_c (on the coarse grid), respectively, with $\Delta x_f < \Delta x_c$. The resolution ratio $R \geqslant 1$ at the discontinuity is then defined as

$$R = \frac{\Delta x_c}{\Delta x_f}. \tag{28}$$

At time $t = 0$, we begin forcing the left boundary with real frequency ω and amplitude A. As a consequence, we observe a wave of the form

$$q(x, t) = A \exp(i(kx - \omega t)) \tag{29}$$

with complex wavenumber $k(\omega)$ satisfying $\text{Im}(k) \geqslant 0$ (under sufficient stability conditions).
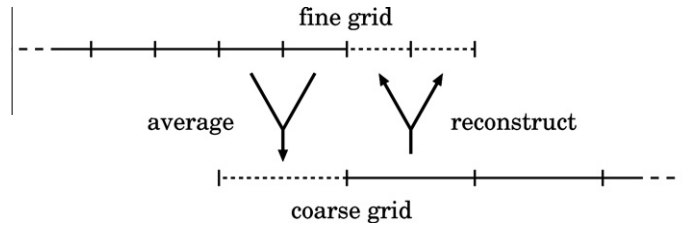
Fig. 5. We maintain the illusion of resolution regularity by averaging from the fine grid to coarse grid ghost elements. To obtain the cell-averaged values on the fine grid, we first construct a sub-grid-scale reconstruction on the coarse grid and then integrate it to obtain the cell-averages on the fine grid. The dotted (overlapping) regions contain the so-called ghost cells.

When running simulations, the resolution discontinuity is treated much like any other boundary on a uniform resolution domain (see Fig. 5). On both the fine and coarse grid the boundary conditions at this point must be obtained from the overlapping grid panel. As a consequence, we are able to maintain the illusion of grid resolution uniformity during the simulation, as long as the boundary conditions are correctly applied.

In order to obtain element-averages for the coarse grid ghost elements that are consistent with the fine grid, we simply average from the fine grid elements. To obtain element-averages on the fine grid from the coarse grid, we first build a sub-grid-scale reconstruction of the form (23) using the element-averaged values from the fine grid and known coarse grid element-averages. Piecewise-linear and piecewise-constant reconstructions can alternatively be obtained by setting one or both of $D q_j$ or $D^2 q_j$ to zero. Then for each fine-grid ghost cell we average over the corresponding reconstruction. This process easily generalizes to higher-dimensions, and does not require any additional special treatment of elements near the resolution discontinuity.

3.2. Decay of parasitic modes

The decay rate of the reflected wave modes can be determined directly from the discretization. Once the initial perturbations from kick-starting the system have died down the frequency ω becomes invariant. Hence, both the "true wave" and "parasitic wave" must oscillate at frequency ω. To determine all complex wavenumbers k with natural frequency ω, we assume wavelike solutions of the form (29). If we define $\beta = \exp(i k \Delta x)$, unstaggered FV schemes of the form (13) can be reduced to a polynomial of the form

$$(\exp(-i\omega\Delta t) - 1)\beta^{\ell} = \sum_{m=-\ell \cdot s}^{r \cdot s} C_m \beta^{m+\ell}. \tag{30}$$

Hence, this polynomial will have $r \cdot s + \ell \cdot s$ roots that represent all wavenumbers that oscillate at frequency ω. In particular, if we assume sufficient stability conditions, roots with $\mathrm{Im}\,(k) \geqslant 0$ will be decaying modes that are propagated forward by our scheme, whereas roots that satisfy $\mathrm{Im}\,(k) < 0$ will be growing modes that are propagated backwards (these are the so-called "parasitic modes"). In fact, the smaller in magnitude (or closer to zero) we observe for $\mathrm{Im}\,(k)$, the longer the resulting "tail" is from the point of generation. Hence, we define the *dominant parasitic mode* for an FV scheme to be the mode $k(\omega)$ that satisfies (30) with $\mathrm{Im}(k) < 0$ such that for any other parasitic mode k' we have $\mathrm{Im}(k) > \mathrm{Im}(k')$. The *spatial decay rate* of the dominant parasitic mode is then defined as $-\mathrm{Im}(k\Delta x)$. A large positive decay rate leads to a sharp drop-off of the parasitic mode, whereas a small positive decay rate leads to an elongated tail. A decay rate of zero corresponds to a parasitic mode which does not decay away from the resolution discontinuity.

We plot the dominant parasitic mode for various choices of frequency ω in Fig. 6. In general, the complexity of the polynomial (30) prevents us from obtaining any general results in all but the simplest of cases, but we can nonetheless make some observations based on these four schemes:

- In all cases the decay rate appears to be smallest at $\omega = 0$, which is associated with a constant forcing. The decay rate then increases monotonically as ω increases.
- At $\omega = 0$ the decay rate can be derived analytically if we observe that, for the schemes we have analyzed, the dominant parasitic mode is the same if we use the coefficients c_m (see (11)) in place of C_m in (30). In fact, for the two upwind schemes and the SLIM scheme with a forward Euler timestep, the degree of the polynomial (30) is only three. If we further observe that for any consistent scheme $\beta = 1$ (the constant mode) must be a root of (30), then the remaining roots are

$$\beta = \frac{-(c_0 + c_1) \pm \sqrt{(c_0 + c_1)^2 - 4c_1(c_{-1} + c_0 + c_1)}}{2c_1}. \tag{31}$$

Using this formula, we can calculate that the $\omega = 0$ decay rate of the dominant parasitic mode is $1.44 \approx \log(-2 + \sqrt{5})$ for the FV2 scheme, $0.99 \approx \log((-5 + \sqrt{33})/2)$ for the FV3p3 scheme and
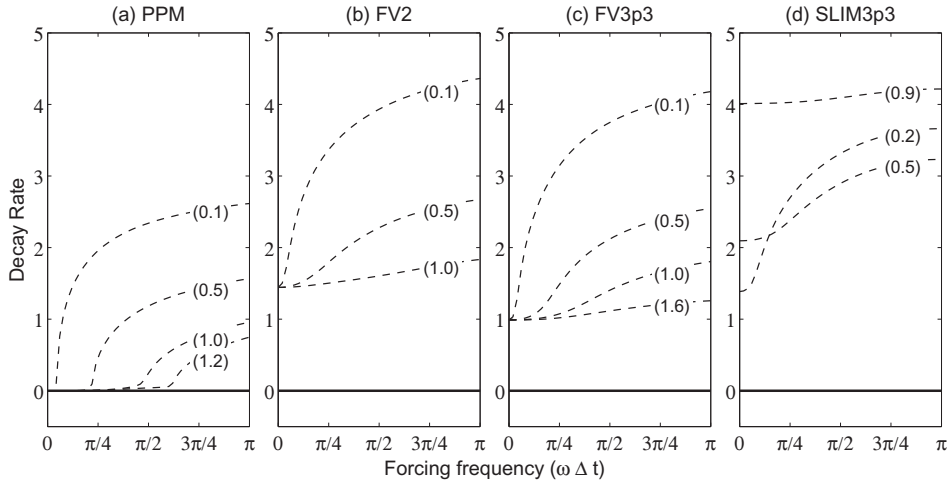
Fig. 6. The decay rate ($-\text{Im}\,(k\Delta x)$) of the dominant parasitic modes for (a) PPM, (b) FV2, (c) FV3p3 and (d) SLIM3p3 under sinusoidal forcing of frequency ω and for several choices of CFL number (indicated in parenthesis on each curve).

$$\beta = \frac{(2K^2 - 3K - 5) - \sqrt{-15K^2 + 18K + 33}}{2(K^2 - 3K + 2)} \tag{32}$$

for the SLIM3p3 scheme. In the limit as $K \rightarrow 1$, the SLIM3p3 scheme does not have any parasitic modes, and so the decay rate tends to infinity. In the limit as $K \rightarrow 0$, the SLIM3p3 scheme converges to a decay rate of $\log((5 + \sqrt{33})/4)$. Observe that since the coefficients c_m are linear in K for the symmetric and upwind FV schemes, all dependence on K divides out of (31).

- For the schemes that use pointwise edge values to calculate edge fluxes (namely, PPM, FV2 and FV3p3), the decay rate decreases monotonically with increasing CFL number at all frequencies $\omega > 0$. At $\omega = 0$, we observe that the decay rate is independent of CFL number.

The number of elements affected by the parasitic mode before it is damped below a fixed threshold is independent of the grid spacing. For a decay rate of 1.44, as with the FV2 scheme, a perturbation at the grid resolution interface of magnitude 1 will require approximately 8 elements to be damped to 10^{-5}. For a decay rate of 0.99, as with the FV3p3 scheme, the same perturbation will require 12 elements to decay to 10^{-5}.

3.3. Amplitude of the parasitic mode at the discontinuity

In addition to knowing the decay rate of a given parasitic mode, it is important to also understand its initial amplitude at a grid resolution discontinuity. To study the amplitude of the parasitic mode, we carried out a sequence of simulations using the PPM scheme at forcing frequencies that were sufficiently low to prevent the parasitic mode from decaying significantly (see Fig. 6). The amplitude of the parasitic mode was calculated empirically by differencing the unrefined and refined grid simulations near the grid resolution discontinuity. This result was then normalized by the amplitude of the incident wave at the discontinuity (since, especially at high wave-numbers, substantial decay of the incident mode was observed).

The empirically calculated ratio of the amplitude of the parasitic mode to the amplitude of the incident wave is depicted in Fig. 7 for various simulations with resolution ratios $R = 2$, 4 and 8. For waves that are well-resolved on both grids, the initial amplitude of the parasitic mode at the discontinuity is largely due to the discrepancy between the "true" solution on the fine grid and the solution in the overlapping grid elements obtained from remapping the coarse grid solution. Improving the order of accuracy in the remapping stage (using a piecewise linear or piecewise parabolic reconstruction, for instance, instead of a piecewise constant reconstruction) will reduce the initial amplitude of the perturbation. For wavenumbers which are poorly resolved or unresolved on the coarse grid, the reconstruction will not carry any information about the "true" wave and so the discrepancy between the incident wave and the representation on the coarse grid will be essentially maximal. In this case, improving the formal accuracy of the remapping procedure will not improve the outcome, since the element averages of the reconstruction on the coarse grid still do not contain any information about these waves.

As observed previously in the literature (see, for example, [37]), wave reflection can be dramatically reduced by smoothly adjusting the grid spacing, rather than through abrupt changes in resolution. Intuitively, this result follows since the sub-grid-scale reconstruction on adjacent grid cells closely matches up under a smoothly varying element width. This result is also consistent with the observations of Trefethen [32], who noted that forcing at the outflow boundary produced parasitic modes of the same amplitude as the prescribed forcing.
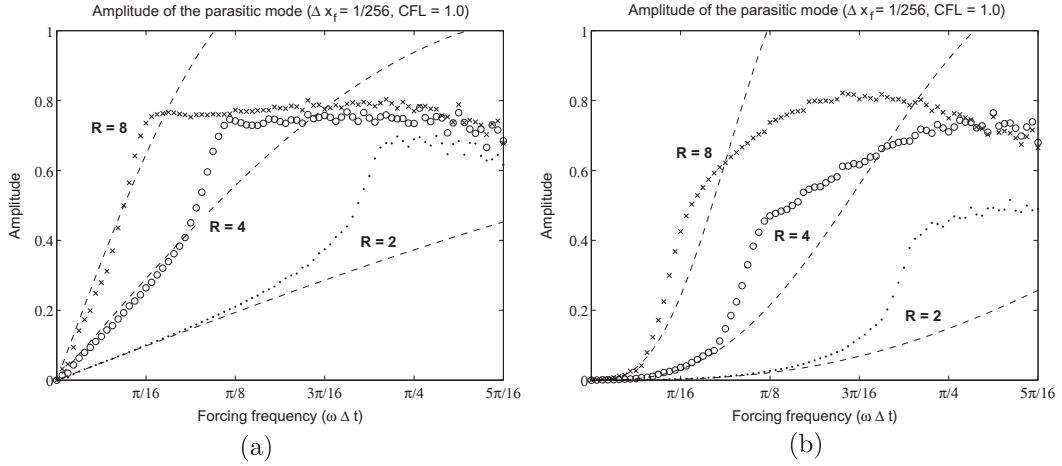
Fig. 7. The amplitude ratio of the parasitic mode for various choices of resolution ratio R and for (a) piecewise constant and (b) piecewise parabolic reconstructions at the grid resolution discontinuity computed from repeated simulations using the PPM scheme. The dashed line indicates the predicted parasitic amplitude from the ideal wave propagation model given by (36), whereas symbols indicate the results of numerical simulation. Observe that the higher-order reconstruction greatly reduces the amplitude ratio at small forcing frequency, but does not substantially affect the reflection amplitude at larger forcing frequencies.

For comparison, we have devised a simple model for predicting the parasitic amplitude. Our goal is to demonstrate that the discrepancy between the solution on the uniform-resolution grid and the solution on the refined grid is the dominant influence in determining the amplitude of the parasitic mode for well-resolved incident waves. Given incident wave solution of the form (29), we can define a moving average operator via

$$\overline{q}(x; R, \Delta x_f) = \frac{1}{R\Delta x_f} \int_x^{x+R\Delta x_f} q(x)dx. \tag{33}$$

If a wave is well-resolved on the fine grid, it will propagate without modification, and so the element average on the fine grid $\overline{q}_f$ will be given by

$$\overline{q}_f = \overline{q}(x; 1, \Delta x_f) = \frac{\exp(i(kx - \omega t))}{k\Delta x_f}(\exp(ik\Delta x_f) - 1). \tag{34}$$

If the wave is well-resolved on the coarse grid as well, the corresponding element average of the first element on the coarse grid $\overline{q}_c$ will be

$$\overline{q}_c = \overline{q}(x; R, \Delta x_f) = \frac{\exp(i(kx - \omega t))}{Rk\Delta x_f}(\exp(iRk\Delta x_f) - 1). \tag{35}$$

For a piecewise-constant reconstruction at the discontinuity, the discrepancy between the true and approximate solution (copied directly from the coarse grid) is then given by

$$D = \overline{q}_f - \overline{q}_c. \tag{36}$$

This approach can be easily extended to higher-order reconstructions (such as we have done with the piecewise-parabolic reconstruction in Fig. 7), but for sake of brevity we have not included the corresponding formula here.

Waves that are not well-resolved on both grids will deviate from the ideal propagation model described above. As frequency is increased, we observe that these wave modes will lead to greater reflection than the ideal model at almost the same frequency for both reconstruction schemes. In fact, if we compare this point of departure with the group velocity plots given in Fig. 1, we observe it is approximately correlated with regions where the group velocity tends away from $u = 1$. Thus, for waves in this moderate-frequency regime, it seems that the numerical method is not able to effectively propagate the energy of the wave away from the discontinuity, implying an increase in the amplitude of the parasitic mode. At high-frequencies the normalized amplitude of the parasitic mode flattens (especially dramatic for the piecewise constant reconstruction), suggesting some maximal efficiency of the reflection process has been achieved. Beyond a forcing frequency of $\omega\Delta t = 5\pi/16$ our empirical analysis method is no longer valid due to the rapid decay rate of the incident mode and apparent decay of the parasitic mode away from the resolution discontinuity.

3.4. Wave reflection by symmetric FV schemes

As observed in Fig. 6, PPM does not significantly damp reflected oscillations at any frequency. This result is apparent in any of the wave-driver simulations using undamped PPM (see Fig. 8). Here we clearly observe a very strong, undamped
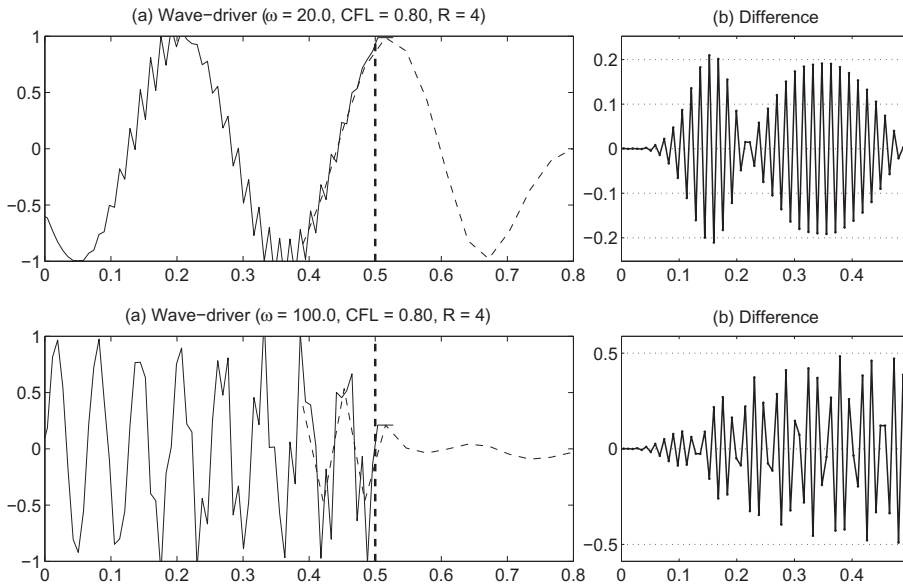
Fig. 8. A wavemaker-driven simulation with PPM, $\Delta x_f = 1/128$, resolution ratio $R = 4$ and $CFL = 0.8$ taken at time $t = 0.75$. The forcing frequency is $\omega = 20.0$ (top) and $\omega = 100.0$ (bottom). A piecewise constant reconstruction is used at the resolution discontinuity ($x = 0.5$, thick dashed line) for remapping from the coarse grid ($x > 0.5$, thin dashed line) to the fine grid ($x < 0.5$, solid line). The simulation results are plotted in (a) and the parasitic mode (obtained from differencing the homogeneous resolution and refined resolution simulations) is plotted in (b). The abscissa represents the x coordinate and the ordinate shows the amplitude (both dimensionless).

high-frequency wave that travels away from the grid resolution interface. The reflected wave has a normalized wavenumber $k\Delta x \approx \pi$ and so travels at a group velocity of $\approx 5/3$ (see Fig. 1). As a consequence, the parasitic mode has almost reached the left boundary by the time the rightgoing wave has only traversed half of the coarse domain.

In agreement with the results in Section 3.3 we see that increasing the order of accuracy of the remapping process at the resolution discontinuity does not significantly affect the qualitative properties of the parasitic wave, and only has an effect on the amplitude of the parasitic wave at smaller wavenumbers (see Fig. 9).

One might wonder if combining this symmetric scheme with a slope/curvature limiter would be sufficient to remove spurious parasitic waves. If we apply the limiting procedure described in [8] we can no longer guarantee continuity at cell edges, and so must utilize a Riemann flux where discontinuities occur. In this case we adopt an upwind flux operator analogous to
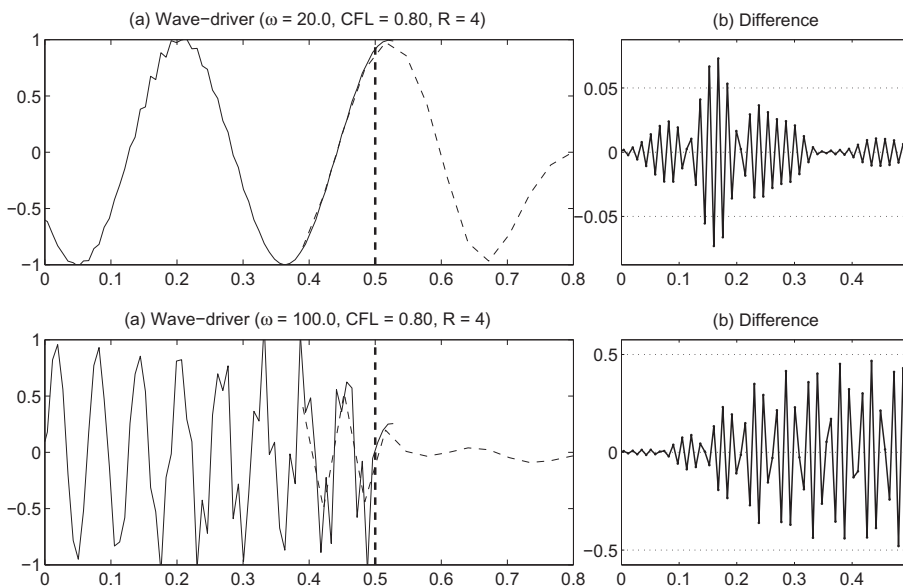
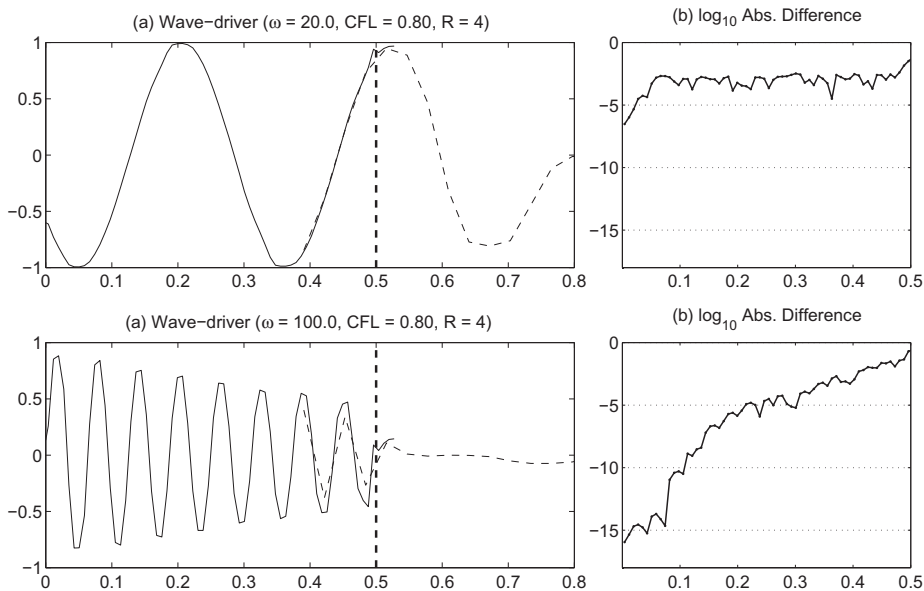**Fig. 9.** As Fig. 8 except with piecewise parabolic reconstruction at the resolution discontinuity.

Fig. 10. As Fig. 9 except with slope/curvature limiter. Note that we have plotted the difference on a logarithmic scale.

(21). Simulations were again carried out using a unlimited piecewise parabolic reconstruction at the resolution discontinuity and are plotted in Fig. 10. The oscillations have been suppressed substantially in this case, but have not been removed completely. In fact, in the small wavenumber case ($\omega = 20.0$) we clearly see that the parasitic mode is persistent at about 10^{-3} of the magnitude of the initial wave. Here we observe the spurious mode is able to "hide" in the low-frequency incident wave, creating a subtle staircasing effect. Here the incident wave also plays the role of a carrier wave for the parasitic mode, since the parasitic mode would be removed almost immediately by the limiting procedure if no incident wave was present. On the other hand, the parasitic mode decays away when $\omega = 100.0$. These results suggest that this choice of limiter is responsible for some damping of the spurious reflected mode, but is unable to remove it entirely in the presence of a low-frequency carrier wave. Nonetheless limiting is effective at high frequencies where the incident wave does not make an effective carrier.

3.5. Wave reflection by upwind FV schemes

Unlike the symmetric FV schemes, upwind FV schemes strongly damp high-frequency modes. We plot the results of four simulations using the FV2 and FV3p3 schemes with driving frequencies $\omega = 20.0$ and $\omega = 100.0$ in Figs. 11 and 12. We observe that the parasitic mode is present with the same initial amplitude as with PPM, but is quickly damped out. In all cases the decay rate of the parasitic mode agrees well with the theory derived in Section 3.2.

3.6. Wave reflection by SLIM FV schemes

SLIM FV schemes behave similarly to upwind FV schemes, except the decay rate tends to exhibit a more interesting structure. We plot the results of two simulations using the SLIM3p3 schemes with driving frequencies $\omega = 20.0$ and $\omega = 100.0$ in Fig. 13. Again, our predictions for the decay rates from Section 3.2 agree well with the simulations.

4. The 1D shallow-water equations and linearized 1D shallow-water equations

In this section we briefly turn our attention to the 1D shallow-water equations and demonstrate how the previous results for the advection equation can be generalized to this case. Unfortunately, our analysis of the 1D shallow-water equations does not generalize to higher dimensions, as would be relevant for geophysical flows, except for wave modes that encounter a grid resolution discontinuity at a right angle. In the case of a higher-dimensional flow, one must also take into consideration *wave refraction*, which results in the splitting of incident waves into reflected and transmitted components when the wave packet hits a grid resolution discontinuity at an oblique angle. Some analysis of wave refraction was tackled by Cathers amd Bates [5], but the complexity of this problem has largely prevented further study. Nonetheless, we believe that there is value in understanding how our results on pure wave reflection can be generalized to the 1D shallow-water equations.

Traditionally, geophysical flows have been modeled using staggered grids (i.e. with mass and momentum variables stored at different points), since many unstaggered finite-difference approaches admit both spurious $2\Delta x$ modes and, for certain ranges of wavenumber k, lead to group velocities that have the wrong sign relative to the flow field. Such properties are
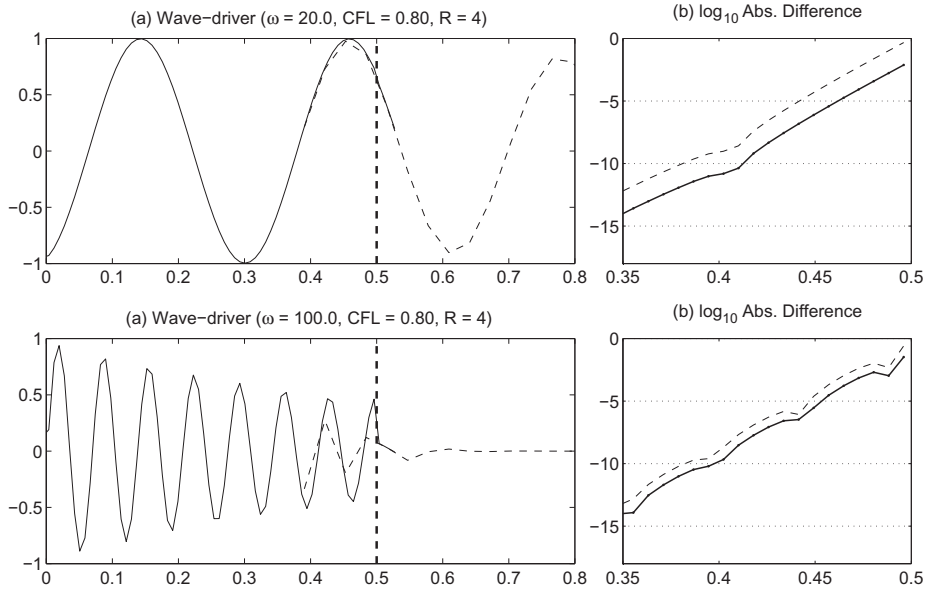
Fig. 11. As Fig. 8 except for the FV2 scheme taken at time t = 1.0. The decay rate predicted in Section 3.2 is shown as a dashed line in (b). Note the shorter horizontal range in (b).
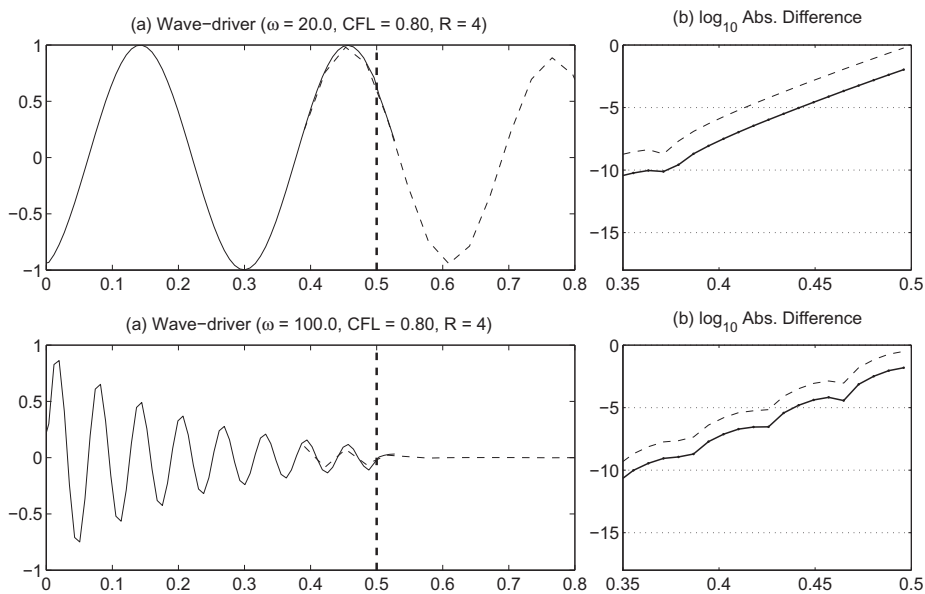
Fig. 12. As Fig. 11 except for the FV3p3 scheme.

absent in certain staggered discretizations. Previously, these problems with unstaggered schemes have been pointed out by Fox-Rabinovitz [10] and Randall [26]. These results have led to a widespread adoption of staggered grids in geophysical flow models that make use of both finite-difference or finite-volume discretizations (see [3,21,25,27,31]). For example, C-grid discretizations have desirable inertio-gravity wave dispersion characteristics. Unfortunately, not all of the attractive properties of staggered schemes on uniform grids carry over to refined grids with a resolution discontinuity. As observed by Chin and Hedstrom [7] and more recently by Frank and Reich [12], although staggered grids do not admit spurious backwards-propagating high-frequency modes, coupling of left- and right-going wave solutions leads to the generation of spurious physical modes at the point of grid refinement (see also Appendix A). As argued by Harris and Durran [15], filters are generally required to maintain accuracy near refinement boundaries. Unstaggered schemes are potentially more desirable in this case, since upwind variants of unstaggered schemes implicitly filter spurious reflections.
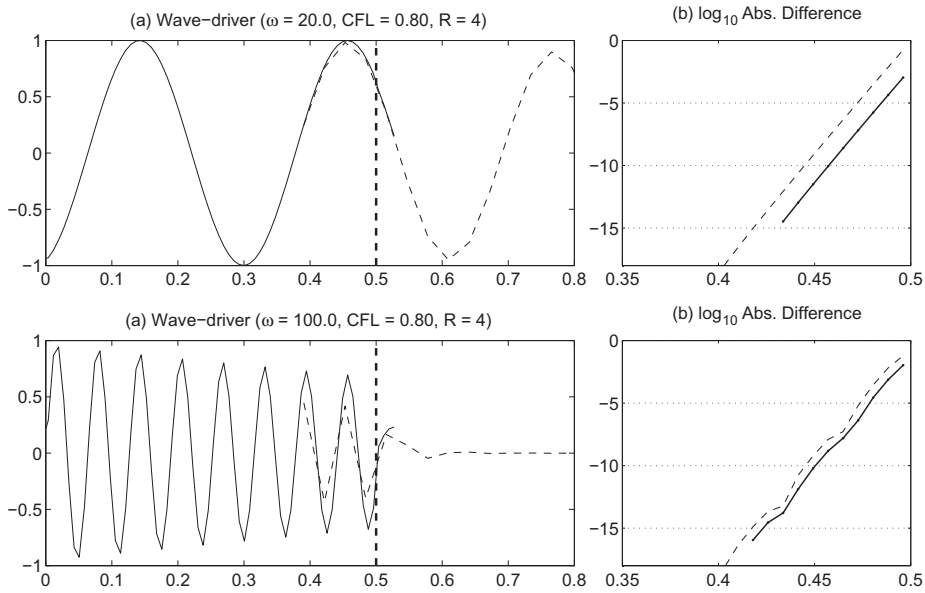
Fig. 13. As Fig. 11 except for the SLIM3p3 scheme.

To begin, we consider the 1D shallow-water equations in conservative form:

$$\frac{\partial h}{\partial t} = -\frac{\partial m}{\partial x},$$ (37)

$$\frac{\partial m}{\partial t} = -\frac{\partial}{\partial x}\left(\frac{m^2}{h} + \frac{1}{2}gh^2\right),$$ (38)

where h is the total height, $m = h\,u$ is the momentum and g is the gravitational constant. If we consider only linearized wave motions on a constant background height field H,

$$h = H + h', \quad \text{and} \quad m = m',$$ (39)

(where the prime denotes the deviations from the background fields) then the 1D shallow-water equations reduce to the linearized 1D shallow-water equations,

$$\frac{\partial h'}{\partial t} = -\frac{\partial m'}{\partial x},$$ (40)

$$\frac{\partial m'}{\partial t} = -gH\frac{\partial h'}{\partial x}.$$ (41)

The linearized 1D shallow-water equations support wave-like solutions of the form

$$\mathbf{q}(x,t) = \hat{\mathbf{q}}\exp(i(kx - \omega t)),$$ (42)

where $\mathbf{q} = [h, m]$ is the state vector with amplitudes $\hat{\mathbf{q}} = [\hat{h}, \hat{m}]$. On substituting this relation into (40) and (41), we obtain

$$\underbrace{\begin{bmatrix} -i\omega & ik \\ gHik & -i\omega \end{bmatrix}}_{M} \begin{bmatrix} \hat{h} \\ \hat{m} \end{bmatrix} = 0.$$ (43)

Hence, in order for wave solutions to exist, we must have det $(M) = 0$, which implies a dispersion relation of the form

$$\omega = \pm k\sqrt{gH},$$ (44)

corresponding to a rightgoing mode ($\omega > 0$) and a leftgoing mode ($\omega < 0$), for each positive wave number. The quantity $\sqrt{gH}$ is the shallow-water gravity wave speed.

4.1. Riemann invariants

The full 1D shallow-water equations admit two Riemann invariants, denoted $\mathcal{L}$ and $\mathcal{R}$, of the form

$$\mathcal{L} = \frac{m}{h} - 2\sqrt{gh}, \quad \text{and} \quad \mathcal{R} = \frac{m}{h} + 2\sqrt{gh}. \tag{45}$$

These are propagated according to

$$\frac{\partial \mathcal{L}}{\partial t} + \left(\frac{m}{h} - \sqrt{gh}\right)\frac{\partial \mathcal{L}}{\partial x} = 0, \quad \frac{\partial \mathcal{R}}{\partial t} + \left(\frac{m}{h} + \sqrt{gh}\right)\frac{\partial \mathcal{R}}{\partial x} = 0 \tag{46}$$

with only weak coupling between these modes due to the nonlinear wave speed (the parenthesized terms in (46)). Observe that for subcritical flow $m/h < \sqrt{gh}$, these modes are propagated leftward and rightward, respectively.

The linearized 1D shallow-water equations admit a leftgoing Riemann invariant $\mathcal{L}'$ and a rightgoing Riemann invariant $\mathcal{R}'$, defined in terms of h' and m' as

$$\mathcal{L}' = \frac{m'}{\sqrt{gH}} - h', \quad \text{and} \quad \mathcal{R}' = \frac{m'}{\sqrt{gH}} + h'. \tag{47}$$

The evolution of these quantities is then described by

$$\frac{\partial \mathcal{L}'}{\partial t} - \sqrt{gH}\frac{\partial \mathcal{L}'}{\partial x} = 0, \quad \frac{\partial \mathcal{R}'}{\partial t} + \sqrt{gH}\frac{\partial \mathcal{R}'}{\partial x} = 0, \tag{48}$$

which is exactly the leftgoing and rightgoing advection equation with wave speed $\sqrt{gH}$.

Thus, for the subcritical shallow-water equations or linearized shallow-water equations we only obtain a well-posed system of equations if we specify the rightgoing Riemann invariant $\mathcal{R}$ at the left boundary and the leftgoing Riemann invariant $\mathcal{L}$ at the right boundary.

The main problem in generalizing the results for the 1D shallow-water equations to higher dimensions arises largely with the Riemann invariants, which are not well defined for higher-dimensional systems.

4.2. Numerical discretizations

The numerical discretizations introduced in Section 2 can be easily formulated for the linearized 1D shallow-water equations. The SLIM scheme can also be generalized to the linearized 1D shallow-water equations by operating on Riemann invariants, but adapting this scheme to the full non-linear shallow-water equations is not immediately obvious. For this reason, in this section we will concentrate our efforts on the symmetric and upwind finite-volume schemes.

The gas-dynamics form of the PPM scheme (see Section 2.4) for the 1D linearized shallow-water equations takes on the semi-discretization

$$\frac{\partial h_j}{\partial t} = -\left[\frac{m_{j-2} - 8m_{j-1} + 8m_{j+1} - m_{j+2}}{12\Delta x}\right], \tag{49}$$

$$\frac{\partial m_j}{\partial t} = -gH\left[\frac{h_{j-2} - 8h_{j-1} + 8h_{j+1} - h_{j+2}}{12\Delta x}\right]. \tag{50}$$

The familiar centered-difference operators are apparent on the right-hand-side of this formulation.

The upwind FV2 scheme (see Section 2.5), on the other hand, takes on the semi-discretization

$$\frac{\partial h_j}{\partial t} = -\left[\frac{m_{j-2} - 6m_{j-1} + 6m_{j+1} - m_{j+2}}{8\Delta x}\right] + \frac{\Delta x^3 \sqrt{gH}}{8}\left(\frac{-h_{j-2} + 4h_{j-1} - 6h_j + 4h_{j+1} - h_{j+2}}{\Delta x^4}\right), \tag{51}$$

$$\frac{\partial m_j}{\partial t} = -gH\left[\frac{h_{j-2} - 6h_{j-1} + 6h_{j+1} - h_{j+2}}{8\Delta x}\right] + \frac{\Delta x^3 \sqrt{gH}}{8}\left(\frac{-m_{j-2} + 4m_{j-1} - 6m_j + 4m_{j+1} - m_{j+2}}{\Delta x^4}\right). \tag{52}$$

We observe that this method combines an $O(\Delta x^3)$ approximation to the advective term (first term on the RHS) with a diffusion term proportional to the fourth-derivative of the field (second term on the RHS). This combination of advective and diffusive terms is typical for upwind-type methods.

Finally, the upwind FV3p3 scheme (see Section 2.6) has semi-discretization

$$\frac{\partial h_j}{\partial t} = -\left[\frac{m_{j-2} - 8m_{j-1} + 8m_{j+1} - m_{j+2}}{12\Delta x}\right] + \frac{\Delta x^3 \sqrt{gH}}{12}\left(\frac{-h_{j-2} + 4h_{j-1} - 6h_j + 4h_{j+1} - h_{j+2}}{\Delta x^4}\right), \tag{53}$$

$$\frac{\partial m_j}{\partial t} = -gH\left[\frac{h_{j-2} - 8h_{j-1} + 8h_{j+1} - h_{j+2}}{12\Delta x}\right] + \frac{\Delta x^3 \sqrt{gH}}{12}\left(\frac{-m_{j-2} + 4m_{j-1} - 6m_j + 4m_{j+1} - m_{j+2}}{\Delta x^4}\right). \tag{54}$$

Here we observe that (53) is identical to (51), except with the $O(\Delta x^3)$ approximation to the first-derivative term replaced by a more accurate $O(\Delta x^4)$ approximation on the same stencil and with a slightly weaker diffusion term. Further, comparing with (49), we observe that this scheme has an identical advective component, and only differs in the addition of a diffusive term.

4.3. Leftgoing and rightgoing mode separation

As we see in Eqs. (49)–(54), unstaggered linear finite-volume schemes lead to semi-discretizations of the linearized shallow-water equations that take the form

$$\frac{\partial h_j}{\partial t} = -\left(\sum_{a=-\ell}^{r} c_a m_{j+a}\right) + \sum_{a=-\ell}^{r} d_a h_{j+a}, \tag{55}$$

$$\frac{\partial m_j}{\partial t} = -gH\left(\sum_{a=-\ell}^{r} c_a h_{j+a}\right) + \sum_{a=-\ell}^{r} d_a m_{j+a}, \tag{56}$$

where the coefficients c_a and d_a are constant in h and m, but are a function of the grid spacing Δx and wave speed $\sqrt{gH}$ (and should not be confused with the coefficients of the advection Eq. (11)). Here ℓ and r again denote the number of leftward-elements and rightward-elements in the stencil. Hence, under a linear timestepping operator, the discretizations (55) and (56) lead to an evolution equation for the leftgoing Riemann invariant $\mathcal{L}'_j$ given by

$$\frac{\partial \mathcal{L}'_j}{\partial t} = \sqrt{gH}\left(\sum_{a=-\ell}^{r} c_a \mathcal{L}'_{j+a}\right) + \sum_{a=-\ell}^{r} d_a \mathcal{L}'_{j+a}. \tag{57}$$

Similarly, the evolution equation for the rightgoing Riemann invariant $\mathcal{R}'_j$ is given by

$$\frac{\partial \mathcal{R}'_j}{\partial t} = -\sqrt{gH}\left(\sum_{a=-\ell}^{r} c_a \mathcal{R}'_{j+a}\right) + \sum_{a=-\ell}^{r} d_a \mathcal{R}'_{j+a}. \tag{58}$$

First, observe that as long as the discretization of the temporal derivative is linear with respect to the spatial derivative (such as from an Eulerian or Runge–Kutta timestepping scheme) these equations have decoupled from one another. Second, observe that these equations are simply the discretization of the advection equation associated with the same discrete spatial operator as in (55). This result implies that our analysis of the advection equation in Section 3.1 should also apply to the 1D linearized shallow-water equations, and hence our analysis should accurately describe the dominant forcing mechanism for parasitic waves in the full 1D shallow-water equations.

4.4. Wave reflection due to coupling of Riemann invariants

Unlike the advection equation, the shallow-water system can generate spurious waves at a grid resolution discontinuity by artificially transferring energy between Riemann invariants. The 1D shallow-water equations, and their linear counterparts admit both leftgoing and rightgoing Riemann invariants for the case of subcritical flow. A grid resolution discontinuity can trigger an interaction between these modes which results in a spurious transfer of energy between one or more Riemann invariants. On the unstaggered grid, wave reflection of this type does not arise in discretizations of the 1D linearized shallow-water equations, but does arise in the nonlinear shallow-water equations due to the aforementioned weak coupling of Riemann invariants (see Section 4.1).

The amplitude of these spurious physical modes is strongly dependent on the degree of nonlinearity present in the system, which can be characterized via the shallow-water Froude number,

$$Fr = \frac{u'}{\sqrt{gh}}, \tag{59}$$

where u' denotes the perturbation from some mean velocity. Systems with larger Froude number have a greater tendency to lead to abruptly varying flows (such as breaking waves) that are more strongly reflected. In general, repeated simulations have shown that the amplitude of a spurious physical mode generated by interaction of Riemann invariants will increase on coarser grids (larger Δx) and increasing resolution ratio R. For a flow with a Froude number of 0.1, we have observed that sharp gradients can readily lead to accumulated errors in the "backwards" propagating Riemann invariant on the order of 1%.

5. Conclusions

In this paper we have considered symmetric, upwind and semi-Lagrangian integrated mass (SLIM) numerical discretizations of the 1D advection equation in the presence of an abrupt discontinuity in grid resolution. We have presented approaches for characterizing the initial amplitude of a parasitic mode as well as its decay rate away from a grid resolution discontinuity. An analysis of the diffusion and group velocity of the upwind and SLIM schemes has revealed that upwind

schemes largely remove any spurious modes that would normally be carried "backwards" relative to the flow. Unstaggered symmetric schemes, on the other hand, do not damp the parasitic modes, which must be dealt with through some alternative mechanism. We have also examined symmetric schemes which have been combined with a typical slope/curvature limiter, but found that although this strategy is effective at removing oscillations in the high-frequency regime, the parasitic mode is retained for relative low-frequencies. Tests using high-order accurate reconstructions at the grid resolution discontinuity have shown that although increasing the order of accuracy of the reconstruction is effective for low-frequency modes, at high-frequencies parasitic modes are again retained.

The 1D shallow-water equations were also considered briefly. Although staggered discretizations have typically been used in the context of geophysical flows, it has been argued that these schemes are unsuitable in the presence of an abrupt resolution discontinuity, since they trigger spurious physical modes which are difficult to remove (additional details are presented in Appendix A and Frank and Reich [12]). In the 1D case, the unstaggered schemes we have considered have the benefit of decoupling leftgoing and rightgoing Riemann invariants, and so our analysis of the advection equation can be applied directly.

Clearly, spurious wave reflection due to an abrupt grid resolution discontinuity is a significant problem that can result in severe degradation of the performance of any numerical method. Hence, some mechanism must be present in order to remove contamination by these modes. For symmetric schemes this mechanism likely should come in the form of an explicit diffusion term, which is naturally present in upwind schemes. With this additional diffusion term, upwind schemes perform very well at damping out reflected oscillations for the linear equations. Nonetheless, proper care must be taken for the treatment of nonlinear effects which can also lead to the generation of spurious physical modes.

Acknowledgments

Appendix A. A brief note on staggered FV schemes for the linear shallow-water equations

Strict conservation of momentum is sometimes unnecessary and external forcing from source terms-especially in the context of geophysical flows-often prevents exact conservation. Hence, it has become common practice (see, for instance, [22,24]) to combine a finite-volume scheme for the mass variable (in this case h) with a finite-difference scheme for the momentum component. Further, due to the resulting beneficial numerical properties (see, for example, [26]), velocity points are typically placed along edges of the height volumes. This combination leads us to a family of staggered grid schemes based on the finite-volume framework.

The most basic staggered FV scheme is the so-called second-order central-in-space (CiS) scheme. Under this scheme, the height and momentum evolution equations satisfy the semi-discretization

$$\frac{\partial h_j}{\partial t} = -\left[\frac{m_{j+1/2} - m_{j-1/2}}{\Delta x_j}\right], \tag{A.1}$$

$$\frac{\partial m_{j+1/2}}{\partial t} = -gH\left[\frac{h_{j+1} - h_j}{\Delta x_{j+1/2}}\right]. \tag{A.2}$$

As with the symmetric FV scheme, the eigenvalues of this semi-discretization are purely imaginary, and so must be paired with at least a third-order Runge–Kutta timestepping operator. If we do so, we obtain a scheme which is stable up to a CFL number of approximately 0.866.

The grid resolution discontinuity is more problematic for staggered schemes, since the momentum is stored pointwise at the grid discontinuity. In order to maintain high-order accuracy consistent with the CiS scheme, we require a $O(\Delta x^2)$ reconstruction for $\partial h/\partial x$ that cannot be obtained by simply using neighboring element-averages of h. For a discontinuity with resolution ratio $R \geqslant 1$, left-grid width Δx_f and right-grid width $\Delta x_c = R\Delta x_f$, we find that the momentum satifies

$$\frac{\partial m_{N+1/2}}{\partial t} = -gH\frac{R}{\Delta x_c(2+R)(1+R)}\left[(1-R^2)h_{N-1} - (7-R^2)h_N + 6h_{N+1}\right] + O(\Delta x_c^2), \tag{A.3}$$

where index $N + 1/2$ corresponds to the position of the resolution discontinuity.

The main problem with using a staggered scheme in combination with an abrupt grid resolution discontinuity can be observed directly from numerical experiments. We plot two such experiments in Fig. A.14. Unlike with unstaggered schemes, the staggered finite-volume discretizations do not have decoupled Riemann invariants, and so allow energy to be transferred between leftgoing and rightgoing waves. This interaction is strongly dependent on the choice of boundary reconstruction and timestep scheme, since these two factors determine which wavenumbers are available at a given frequency. At high-frequencies the scheme is unable to transfer energy into the forward-propagating mode on the coarse grid (since the wave cannot be resolved in this region) and so must transfer this energy into a backward-propagating mode. As a result, we observe that at high-frequencies most of the energy of the incident wave translates into a backwards-propagating mode.
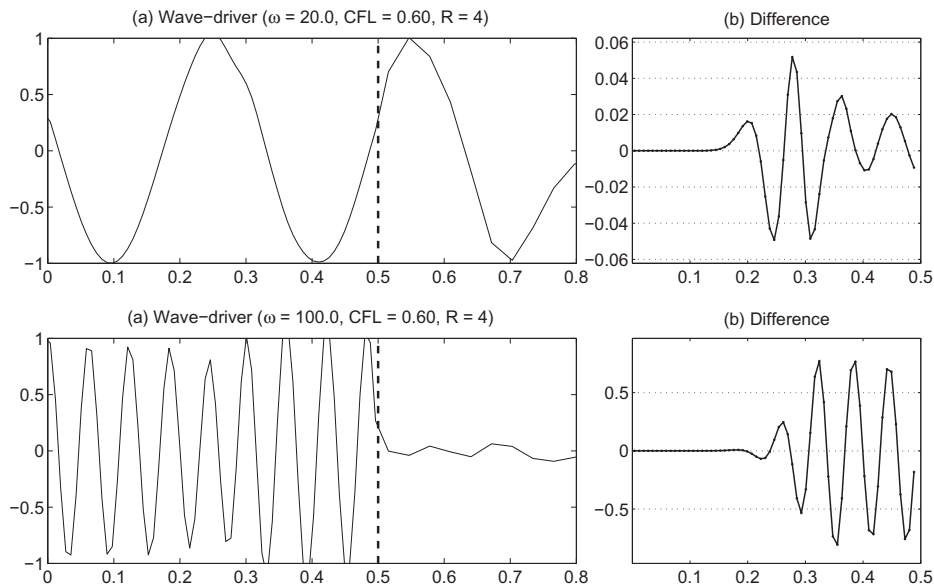
Fig. A.14. A wavemaker-driven simulation with the second-order CiS scheme with $\Delta x_f = 1/128$, resolution ratio $R = 4$ and $CFL = 0.6$. The forcing frequency is $\omega = 20.0$ (top) and $\omega = 100.0$ (bottom). The simulation results at $t = 0.8$ are plotted in (a) and the parasitic mode (obtained from differencing the homogeneous resolution and refined resolution simulations) is plotted in (b). The abscissa represents the x coordinate and the ordinate shows the amplitude of h (both dimensionless).

Observe that in Fig. A.14 (top) the parasitic mode does not appear to have the same wavelength as the incident wave. In fact, the accuracy of the reconstruction at the grid refinement boundary significantly reduces the reflection error, and so the error associated with the wave front initially hitting the grid refinement boundary appears enhanced. It takes roughly until $t = 2.0$ before the wavelength of the reflected wave settles to that of the incident wave. A similar numerical experiment using a reconstruction analogous to (A.2) at the discontinuity (note that such a reconstruction is first-order at this point) nearly immediately produces a parasitic mode with wavelength equal to the incident wave.

Coupling of wave modes in the staggered scheme described in this section suggests that the reflected mode is almost indistinguishable from an incident physical mode. As a consequence, filters that remove high-frequency Fourier modes near the resolution discontinuity will not be able to detect these waves.

From these observations we conclude that staggered schemes that are constructed similar to the one described above are unsuitable for application on grids that have an abrupt grid resolution discontinuity. A thorough analysis of staggered schemes on a refined grid has been given by Long [23].

References

[1] M.J. Berger, P. Colella, Local adaptive mesh refinement for shock hydrodynamics, J. Comput. Phys. 82 (1989) 64–84.
[2] M.J. Berger, J. Oliger, Adaptive mesh refinement for hyperbolic partial differential equations, J. Comput. Phys. 53 (1984) 484–512.
[3] L. Bonaventura, T. Ringler, Analysis of discrete shallow-water models on geodesic delaunay grids with C-type staggering, Mon. Weather Rev. 133 (2005) 2351–2373.
[4] L. Brillouin, Wave Propagation and Group Velocity, Academic Press, New York, 1960.
[5] B. Cathers, S. Bates, Spurious numerical refraction, Int. J. Numer. Methods Fluids 21 (1995) 1049–1066.
[6] J.G. Charney, R. Fjørtoft, J. von Neumann, Numerical integration of the barotropic vorticity equation, Tellus 2 (1950) 237–254.
[7] R.C.Y. Chin, G.W. Hedstrom, Scattering of waves from a staggered difference scheme on a variable grid, Proceedings of 11th IMACS World Congress, Montreal, Que, IMACS, New Brunswick, NJ, 1982, pp. 49–51.
[8] P. Colella, P.R. Woodward, The piecewise parabolic method (PPM) for gas-dynamical simulations, J. Comput. Phys. 54 (1984) 174–201.
[9] J. Côté, S. Gravel, A. Méthot, A. Patoine, M. Roch, A. Staniforth, The operational CMC MRB global environmental multiscale (GEM) model. Part I: Design considerations and formulation, Mon. Weather Rev. 126 (1998) 1373–1395.
[10] M.S. Fox-Rabinovitz, Computational dispersion properties of horizontal staggered grids for atmospheric and ocean models, Mon. Weather Rev. 119 (1991) 1624–1639.
[11] M.S. Fox-Rabinovitz, L.L. Takacs, R.C. Govindaraju, M.J. Suarez, A variable-resolution stretched-grid general circulation model: regional climate simulation, Mon. Weather Rev. 129 (2001) 453–469.
[12] J. Frank, S. Reich, On Spurious Reflections, Non-uniform Grids and Finite Difference Discretizations of Wave Equations, Technical Report, Center for Mathematics and Computer Science, CWI Report MAS-E0406, (2004).
[13] J.E. Fromm, A method for reducing dispersion in convective difference schemes, J. Comput. Phys. 3 (1968) 176–189.
[14] R. Grotjahn, J.J. O'Brien, Some inaccuracies in finite differencing hyperbolic equations, Mon. Weather Rev. 104 (1976) 180–194.
[15] L.M. Harris, D.R. Durran, An idealized comparison of one-way and two-way grid nesting, Mon. Weather. Rev. 138 (2009) 2174–2187.
[16] C. Jablonowski, M. Herzog, J.E. Penner, R.C. Oehmke, Q.F. Stout, B. van Leer, K.G. Powell, Block-structured adaptive grids on the sphere: advection experiments, Mon. Weather Rev. 134 (2006) 3691–3713.
[17] C. Jablonowski, R.C. Oehmke, Q.F. Stout, Block-structured adaptive meshes and reduced grids for atmospheric general circulation models, Philos. Trans. R. Soc. A 367 (2009) 4497–4522.

[18] S. Karni, On the group velocity of symmetric and upwind numerical schemes, Int. J. Numer. Methods Fluids 18 (1994) 1073–1081.
[19] J.P.R. Laprise, A. Plante, A class of semi-Lagrangian integrated-mass (SLIM) numerical transport algorithms, Mon. Weather Rev. 123 (1995) 553–565.
[20] P.H. Lauritzen, R.D. Nair, P.A. Ullrich, A conservative semi-Lagrangian multi-tracer transport scheme (CSLAM) on the cubed–sphere grid, J. Comput. Phys. 229 (2010) 1401–1424.
[21] S. Lin, A vertically Lagrangian finite-volume dynamical core for global models, Mon. Weather Rev. 132 (2004) 2293–2307.
[22] S. Lin, R.B. Rood, An explicit flux-form semi-Lagrangian shallow-water model on the sphere, Q. J. Roy. Meteorol. Soc. 123 (1997) 2477–2498.
[23] D. Long, Spurious Propagation of Hyperbolic Waves On In-Homogeneously Staggered Grids, Master's Thesis, University of Exeter, U.K. (2009).
[24] J. Marshall, A. Adcroft, C. Hill, L. Perelman, C. Heisey, A finite-volume, incompressible Navier–Stokes model for studies of the ocean on parallel computers, J. Geophys. Res. 102 (1997) 5753–5766.
[25] J.L. McGregor, Geostrophic adjustment for reversibly staggered grids, Mon. Weather Rev. 133 (2005) 1119–1128.
[26] D.A. Randall, Geostrophic adjustment and the finite-difference shallow-water equations, Mon. Weather Rev. 122 (1994) 1371–1377.
[27] G.A. Schmidt, R. Ruedy, J.E. Hansen, I. Aleinov, N. Bell, M. Bauer, S. Bauer, B. Cairns, V. Canuto, Y. Cheng, A. Del Genio, G. Faluvegi, A.D. Friend, T.M. Hall, Y. Hu, M. Kelley, N.Y. Kiang, D. Koch, A.A. Lacis, J. Lerner, K.K. Lo, R.L. Miller, L. Nazarenko, V. Oinas, J. Perlwitz, J. Perlwitz, D. Rind, A. Romanou, G.L. Russell, M. Sato, D.T. Shindell, P.H. Stone, S. Sun, N. Tausnev, D. Thresher, M. Yao, Present-day atmospheric simulations using GISS model E: comparison to in situ, satellite, and reanalysis data, J. Clim. 19 (Jan.) (2006) 153–192.
[28] W.C. Skamarock, J.B. Klemp, Adaptive grid refinement for two-dimensional and three-dimensional nonhydrostatic atmospheric flow, Mon. Weather Rev. 121 (1993) 788–804.
[29] W.C. Skamarock, J. Oliger, R.L. Street, Adaptive grid refinement for numerical weather prediction, J. Comput. Phys. 80 (1989) 27–60.
[30] A.N. Staniforth, H.L. Mitchell, A variable-resolution finite-element technique for regional forecasting with the primitive equations, Mon. Weather Rev. 106 (1978) 439–447.
[31] J. Thuburn, T.D. Ringler, W.C. Skamarock, J.B. Klemp, Numerical representation of geostrophic modes on arbitrarily structured C-grids, J. Comput. Phys. 228 (22) (2009) 8321–8335.
[32] L.N. Trefethen, Group velocity in finite difference schemes, SIAM Rev. 24 (2) (1982) 113–136.
[33] P.A. Ullrich, C.J. Jablonowski, B.L. van Leer, High-order finite-volume models for the shallow-water equations on the sphere, J. Comput. Phys. 229 (2010) 6104–6134.
[34] B. van Leer, Towards the ultimate conservation difference scheme J. II. Monotonicity and conservation combined in a second-order scheme, Comput. Phys. 14 (1974) 361–370.
[35] B. van Leer, Towards the ultimate conservative difference scheme. IV. A new approach to numerical convection, J. Comput. Phys. 23 (1977) 276–299.
[36] B. van Leer, Towards the ultimate conservative difference scheme. V – A second-order sequel to Godunov's method, J. Comput. Phys. 32 (1979) 101–136.
[37] R. Vichnevetsky, Wave propagation and reflection in irregular grids for hyperbolic equations, Appl. Numer. Math. 3 (1987) 133–166.
[38] R. Vichnevetsky, L.H. Turner, Spurious scattering from discontinuously stretching grids in computational fluid dynamics, Appl. Numer. Math. 8 (3) (1991) 289–299.